Environmental Research 275 (2025) 121301

Contents lists available at ScienceDirect

Environmental Research

journal homepage: www.elsevier.com/locate/envres

S-scheme Bi_2MoO_6/BiOBr heterostructure for effective removal of dye: Synergistic mechanism insight of adsorption-photocatalysis

Lili Ai [*,1], Lijuan Feng [1], Luxiang Wang [**], Yuchun Li, Chuan Tan, Manning Zha, Dianzeng Jia, Nannan Guo

State Key Laboratory of Chemistry and Utilization of Carbon-Based Energy Resources, College of Chemistry, Xinjiang University, Urumqi, 830017, Xinjiang, PR China

ARTICLE INFO

Keywords:
Bi_2MoO_6/BiOBr
S-scheme heterostructure
Synergistic mechanism
Adsorption-photocatalysis

ABSTRACT

The S-scheme Bi_2MoO_6/BiOBr honeycomb heterostructure has been constructed by solvothermal method. The removal ability of dyes and the synergistic effect of adsorption-photocatalysis were investigated. The optimal sample Bi_2MoO_6/BiOBr-2 can remove 99.6% of MB, 98.1% of TC, and 86.3% of RhB within 30 min, and the excellent photocatalytic performance attributes to the collaboration of adsorption and photocatalysis. The Langmuir isotherm model and the pseudo-second-order kinetic curves are followed in the adsorption of MB by Bi_2MoO_6/BiOBr-2. It can be concluded that the adsorption of MB on Bi_2MoO_6/BiOBr is exothermic and spontaneous by adsorption energy calculations. The S-scheme interface transfer effectively promotes the photogenerated carriers transfer and enhances the photocatalytic activity, and the mechanism of adsorption-photocatalysis collaborative removal of pollutants was further proposed. This work has guiding significance for the construction of materials for collaborative removal of pollutants from water by adsorption photocatalysis, and provides a new idea for water pollution control.

1. Introduction

As the rapid development of the society, the environmental pollution problem is becoming more and more serious, among which the dye wastewater has become one of the urgent problems in the field of water treatment due to its high toxicity and poor natural degradation (Singh et al., 2022). Among the various techniques for removing pollutants, adsorption method is simple and low energy consuming (Cai et al., 2017), but it cannot completely mineralize the pollutants. Photocatalytic degradation of dye wastewater is a clean and efficient method (Anwer et al., 2019; Han et al., 2024). Therefore, adsorption-photocatalytic synergistic strategy has been proposed for the treatment of pollutants in wastewater (Bai et al., 2019; Liu et al., 2019). The dye molecules can be adsorbed and gathered to the surface of the catalyst, increasing their chances of reacting with photogenerated electrons and holes, which leads to an accelerated degradation rate of the dye (Cai et al., 2024).

Bismuth oxybromide (BiOBr) is formed by alternating positive and negative charge layers of $[Bi_2O_2]^{2+}$ and Br^-, resulting in an internal electric field that facilitates the separation of photogenerated carriers (Liu et al., 2024). Moreover, it has appropriate bandgap and wide light absorption range, resulting in a promising application in the field of photocatalysis. However, the high combination of photogenerated carriers limits its photocatalytic ability (Li et al., 2024). Studies have shown that constructing heterostructure can improve the photocatalytic performance through interfacial effects and optimization of energy band structure (Ling et al., 2024; Wang et al., 2024). Among them, the S-scheme heterostructure is composed of two redox photocatalysts with different energy levels, whose unique charge transfer mechanism can effectively broaden the light absorption range while also improving the utilization efficiency of photogenerated carriers, it exhibits excellent dye removal performance (Li et al., 2024; Shen et al., 2025). For example, the S-scheme BiOBr/$Zn_2In_2S_5$ heterojunction that can synergistically adsorb-photocatalytic degradation of tetracycline was constructed by Du et al. And the internal electric field can generate the energy band bending effect in the S-scheme heterojunction, which further promotes the photogenerated electron-hole pairs separation efficiency. Among them, 7 wt% BiOBr/$Zn_2In_2S_5$ exhibited high activity, stability and

* Corresponding author.
** Corresponding author.
E-mail addresses: ailili0709@163.com (L. Ai), wangluxiangxju@163.com (L. Wang).
[1] Authors with equal contributions to this work.

https://doi.org/10.1016/j.envres.2025.121301
Received 25 January 2025; Received in revised form 21 February 2025; Accepted 4 March 2025
Available online 11 March 2025

reusability with a synergistic degradation rate up to 97.52% (Du et al., 2022).

In addition, the close contact interfaces that can facilitate electrons transfer, which can be formed in the heterostructure with similar crystal structures and elemental compositions (Zhou et al., 2023). Pang et al. prepared S-scheme $BiOBr/Bi_2WO_6$ heterojunction with photodegradation efficiency up to 92.3%, the improved separation and migration of carriers and the extended lifetime result in significant photocatalytic performance enhancement (Pang et al., 2024). Jv et al. prepared $BiOBr/Bi_2O_2CO_3$ heterojunction for photocatalytic degradation of tetracycline by in situ construction method, efficient charge transfer at the interface leads to a noticeable increase of photocatalytic activity (Jv et al., 2024). Bi_2MoO_6 with similar structure to BiOBr can share the $[Bi_2O_2]^{2+}$ layer and form a tight contact interface to accelerate the carriers separation and migration ability in the Bi_2MoO_6/BiOBr composite. Hence, it is essential to construct Bi_2MoO_6/BiOBr heterojunction for the removal of dye wastewater.

Based on above consideration, S-scheme Bi_2MoO_6/BiOBr heterostructure was prepared by solvothermal method for adsorption-photocatalytic collaborative dye removal. The composition and morphology of the prepared materials were evaluated by methods such as XRD, XPS and SEM. And the photoelectric properties of the samples were studied. The effects of different amount of photocatalyst, pH value and initial concentration of MB on adsorption-photocatalysis and the synergic mechanism of adsorption-photocatalysis were studied in detail by calculations. This study provides a feasible solution to prepare an efficient catalyst for adsorption-photocatalytic synergistic dye removal.

2. Experimental section

2.1. Preparation of the samples

The BiOBr nanoflowers were prepared by solvothermal method. 0.1 mmol $Bi(NO_3)_3{\cdot}5H_2O$ and 0.85 mmol KBr were ultrasonically dispersed in 10 mL glycol until completely dissolved, respectively. The dissolved KBr solution was slowly dripped into $Bi(NO_3)_3{\cdot}5H_2O$ solution and stirred continuously for 0.5 h. Then, the mixed solution was poured into a Teflon-lined high temperature reactor and kept at 160 °C for 10 h. The solid product was obtained by centrifugation, washed three times alternately with ethanol and distilled water, and finally freeze-dried to obtain BiOBr.

The schematic of preparing BiOBr and Bi_2MoO_6/BiOBr composites are shown in Fig. 1a. 0.2 g BiOBr was uniformly dispersed in 30 mL glycol, and 1.3 mmol $Bi(NO_3)_3{\cdot}5H_2O$ was added into the solution and

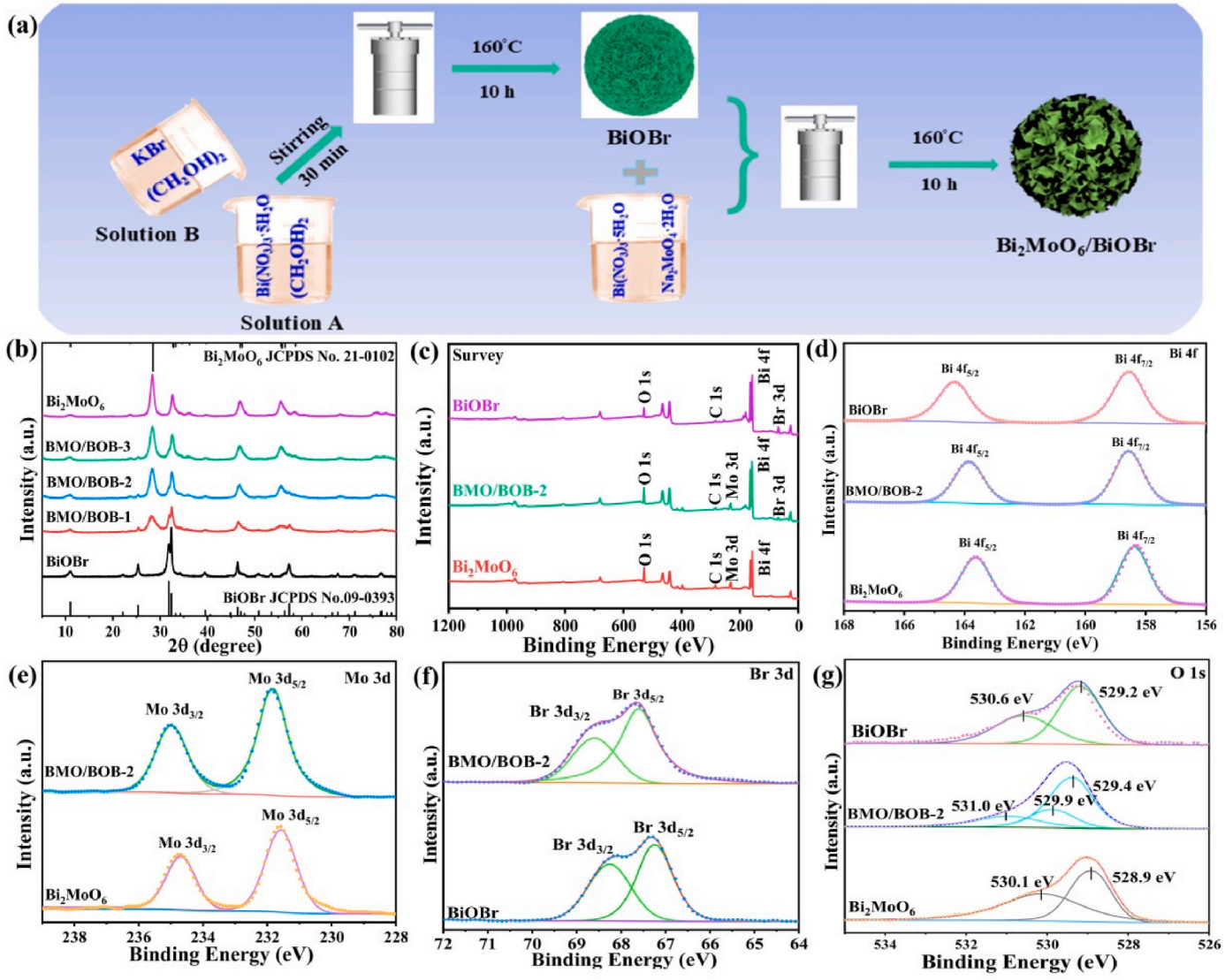

Fig. 1. (a) Schematic synthesis of BiOBr and Bi_2MoO_6/BiOBr composites; (b) XRD patterns of the obtained samples; XPS spectra of Bi_2MoO_6, BiOBr and BMO/BOB-2: (c) survey spectra, (d) Bi 4f, (e) Mo 3d, (f) Br 3d and (g) O 1s.

stirred until completely dissolved. Then, adding a certain amount of $Na_2MoO_4{\cdot}2H_2O$ (0.3 mmol, 0.65 mmol, 0.9 mmol) and continuing to stir for 0.5 h. The mixed solution was poured into a Teflon-lined stainless steel sterilizer and held at 160 °C for 10 h. After the reaction is completed, the obtained product is alternately rinsed with anhydrous ethanol and distilled water and freeze-dried. The prepared Bi_2MoO_6/BiOBr were marked as BMO/BOB-1, BMO/BOB-2, and BMO/BOB-3 according to the dosage of $Na_2MoO_4{\cdot}2H_2O$ with 0.3 mmol, 0.65 mmol, 0.9 mmol. In addition, pure Bi_2MoO_6 was prepared without the addition of BiOBr.

2.2. Characterizations, adsorption experiments and photocatalytic activity test

The characterization techniques for the samples, adsorption experiments and Photocatalytic activity test are shown in the Supporting Information.

3. Results and discussions

3.1. Morphology and structure characterization

The investigation of the crystal structure and phase composition of the synthesized samples were conducted by XRD. Fig. 1b illustrates that the notable diffraction peaks at 31.7°, 32.2°, 46.2° and 57.1° correspond to the (102), (110), (200) and (212) crystal facets of the tetragonal BiOBr (JCPDS No.21-0102) (Sun et al., 2019; Xu et al., 2013), the distinctive diffraction peaks observed at 28.3°, 32.6°, 46.7°, and 55.8° are associated with the (131), (002), (202), and (133) crystal facets of Bi_2MoO_6 (JCPDS No.09-0393) (Ding et al., 2021). The characteristic diffraction peaks of Bi_2MoO_6 and BiOBr appear in the XRD patterns of the prepared compounds. As the content of $Na_2MoO_4{\cdot}2H_2O$ increased, the peaks of Bi_2MoO_6 became stronger. There was no shift and no other impurity peaks appeared in the diffraction peaks of the compound compared with the pure phase, which preliminary proved that the Bi_2MoO_6/BiOBr composite was successfully prepared.

The elemental composition and chemical state of the samples were further validated by XPS characterization. Fig. 1c illustrates that the full spectra of Bi_2MoO_6, BiOBr and BMO/BOB-2. It can be observed that BMO/BOB-2 contains Bi, Br, Mo and O elements. The presence of carbon in the system may be attributed to CO_2 from the atmosphere. The Bi 4f spectrum is presented in Fig. 1d, there are two characteristic peaks at 163.8 eV and 158.5 eV in BMO/BOB-2 belonging to Bi $4f_{5/2}$ and Bi $4f_{7/2}$, respectively, which indicates that the Bi element exists as Bi^{3+} (Wang et al., 2024; Wu et al., 2023). As shown in Fig. 1e, the peaks located at 235.0 eV and 231.9 eV corresponding to Mo $3d_{2/3}$ and Mo $3d_{5/2}$ (Qu et al., 2022; Shen et al., 2022). The Br 3d spectra of BiOBr and BMO/BOB-2 are shown in Fig. 1f. The peaks centered at 68.6 eV and 67.6 eV are attributed to Br $3d_{3/2}$ and Br $3d_{5/2}$ (Lu et al., 2023; Zhao et al., 2023), respectively. Fig. 1g shows the O 1s high-resolution XPS of Bi_2MoO_6, BiOBr, and BMO/BOB-2, the peaks were observed at 529.4 eV and 529.9 eV are associated with the presence of the Bi-O bond. In addition, the peak located at 531.0 eV is related to the adsorbed hydroxyl group on the material (Hu et al., 2018; Xu et al., 2020). The elemental binding energies of the composite all showed significant changes compared to BiOBr and Bi_2MO_6, indicating the presence of

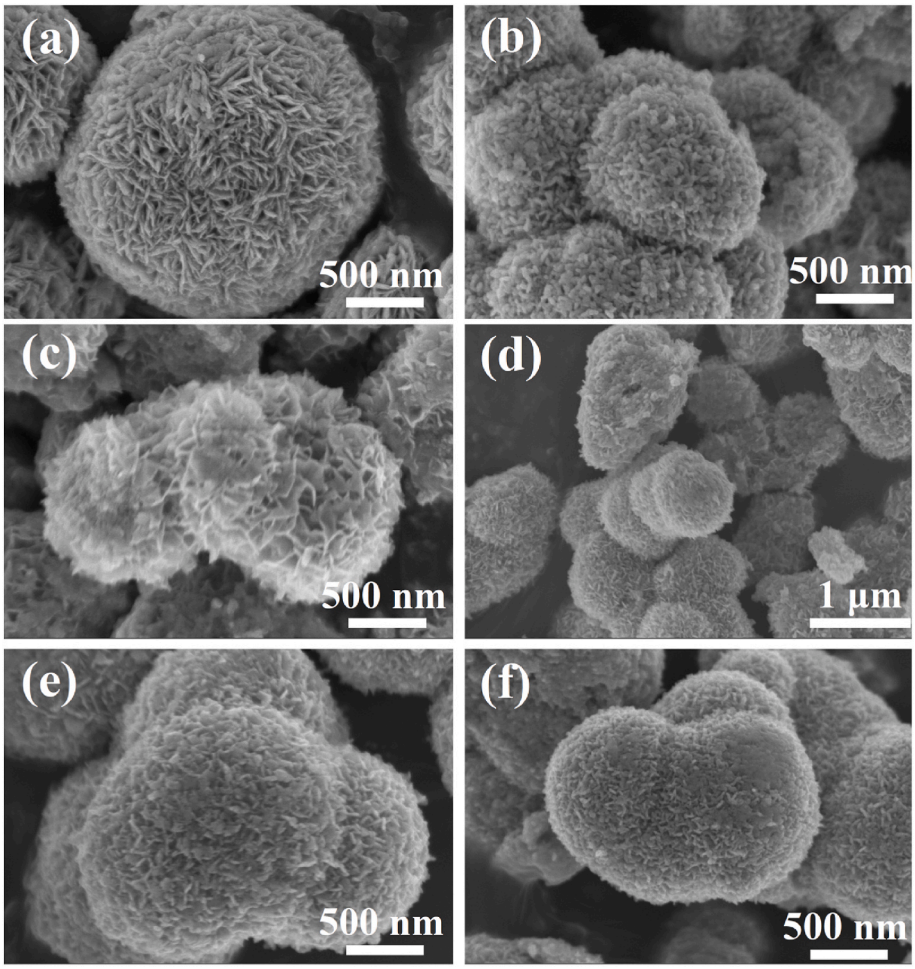

Fig. 2. The SEM images of (a) BiOBr, (b) Bi_2MoO_6, (c) BOB/BMO-1, (d–e) BOB/BMO-2 and (f) BOB/BMO-3.

interactions between Bi_2MoO_6 and BiOBr in the composite. In summary, XPS results further prove that Bi_2MoO_6 and BiOBr coexist in the BMO/BOB-2 composite, which is consistent with XRD results.

The microstructure of the synthesized samples was examined by SEM. It can be seen that BiOBr is composed of two-dimensional nanosheets (Fig. 2a), which are polymerized into a flower-spherical structure of about 1 μm in diameter. This configuration boasts a significant specific surface area, enhancing the material's catalytic and adsorption characteristics. Bi_2MoO_6 shows nanoflowers morphology assembled with nanosheets and the spherical nanoflowers exhibit a diameter about 500 nm (Fig. 2b). The addition of $Na_2MoO_4{\cdot}2H_2O$ can change the thickness of BiOBr nanosheets and form a honeycomb structure. The thickness of the nanosheets is thinner and the honeycomb structure is not evenly distributed when the amount of $Na_2MoO_4{\cdot}2H_2O$ is small (Fig. 2c). With the increase of the content of $Na_2MoO_4{\cdot}2H_2O$, the honeycomb structure is evenly distributed and the contact between the two-dimensional nanosheets is closer (Fig. 2d and e). However, the honeycomb structure showed agglomeration phenomenon because the increase of $Na_2MoO_4{\cdot}2H_2O$ content promoted the nucleation rate of Bi_2MoO_6 when $Na_2MoO_4{\cdot}2H_2O$ was continued to increase (Fig. 2f). The SEM result demonstrate that the morphology formation process of the Bi_2MoO_6/BiOBr composite.

DRS can be used to evaluate the light absorption properties of synthetic samples. In Fig. 3a, the absorption edges for Bi_2MoO_6 and BiOBr are 508 nm and 454 nm, respectively, indicating that both exhibit strong response to visible light (Dong et al., 2024). However, the absorption edge of BiOBr is smaller than that of Bi_2MoO_6, which is caused by a wider band gap. For the Bi_2MoO_6/BiOBr composite, the absorption edge is redshifted with the addition of $Na_2MoO_4{\cdot}2H_2O$, the light absorption capacity of the samples was significantly improved, allowing them to absorb a wider spectrum of wavelengths. Moreover, the absorption threshold of the samples was expanded and the ability to capture light energy is enhanced. The E_g of Bi_2MoO_6 is 2.75 eV, while BiOBr has a slightly higher E_g of 2.94 eV (Fig. 3b). The flat band potential of the material is determined by Mott-Schottky curves. Figs. 3c–d present the Mott-Schottky curves of Bi_2MoO_6 and BiOBr, respectively. The intersection of the tangent to the curve and the horizontal coordinate is the flat charged potential of the sample, thus the flat-band potentials of Bi_2MoO_6 and BiOBr are −0.60 eV and −0.92 eV, respectively. While the conduction-band potentials (E_{CB}) are −0.40 eV and −0.72 eV, respectively (Kang et al., 2023). The band structures of the two catalysts are shown insert of Figs. 3c–d. In summary, Bi_2MoO_6 and BiOBr have suitable band structures, which can form heterostructure. The tight contact interface of the heterojunction can inhibit the combination of electron-hole pairs and effectively facilitate the sample adsorption-photocatalytic synergistic reaction.

The steady-state fluorescence spectroscopy was used to evaluate the recombination efficiency of the electron-hole pairs in the samples. The fluorescence intensity of Bi_2MoO_6/BiOBr composites was significantly decreased compared to Bi_2MoO_6 and BiOBr (Fig. 4a). Of these, the lowest fluorescence intensity was observed for BMO/BOB-2, suggesting that it has the lowest carriers recombination efficiency. And the separation efficiency of photogenerated carriers can be analyzed by photocurrent test, the transient photocurrent curves show that the photoresponse and photocurrent densities of the samples were stable, and the highest photocurrent density was observed for BMO/BOB-2, indicating that its good photocatalytic activity. It means that the formation of heterojunction is important for increasing the interface charge transport rate and extending the carriers lifetime (Fig. 4b). In addition, electrochemical impedance indirectly reflects the transfer rate of charge at the interface. In Fig. 4c, the order of the slope of the EIS curves is Bi_2MoO_6 > BiOBr > BMO/BOB-1 > BMO/BOB-3 > BMO/BOB-2, indicating that the photocatalytic activity of BMO/BOB-2 is superior to other catalysts. Therefore, the formation of Bi_2MoO_6/BiOBr heterojunction can facilitate the migration rate of carriers, and enhance the light absorption, thus improving its activity.

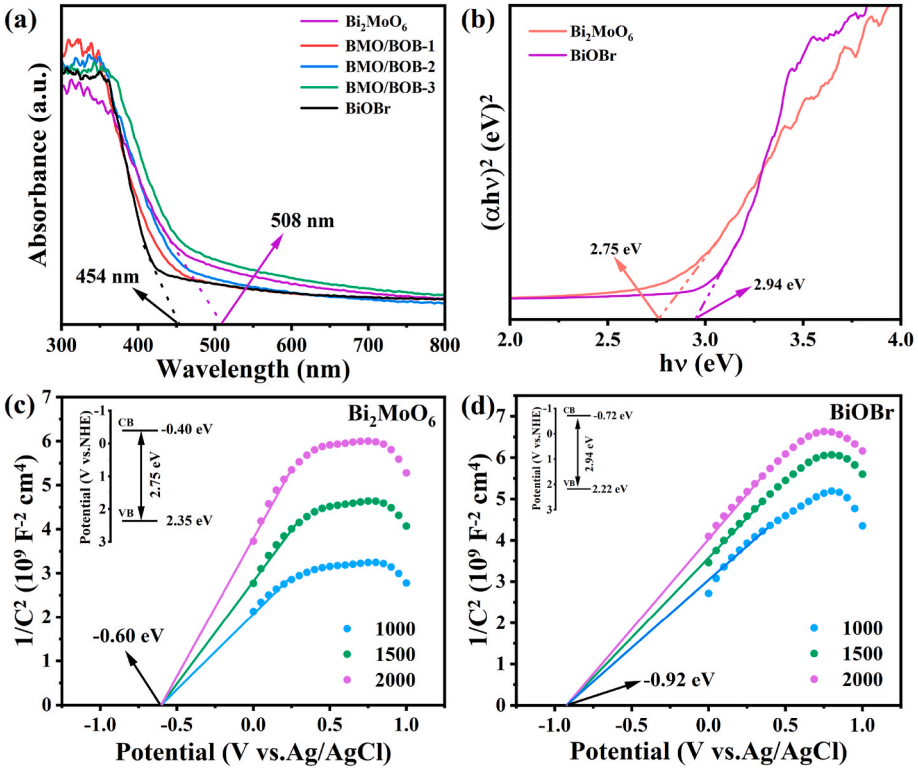

Fig. 3. (a) UV–vis diffuse reflectance spectra of the prepared samples; (b) The band gap widths of Bi_2MoO_6 and BiOBr; Mott-Schottky curves of (c) Bi_2MoO_6 and (d) BiOBr.

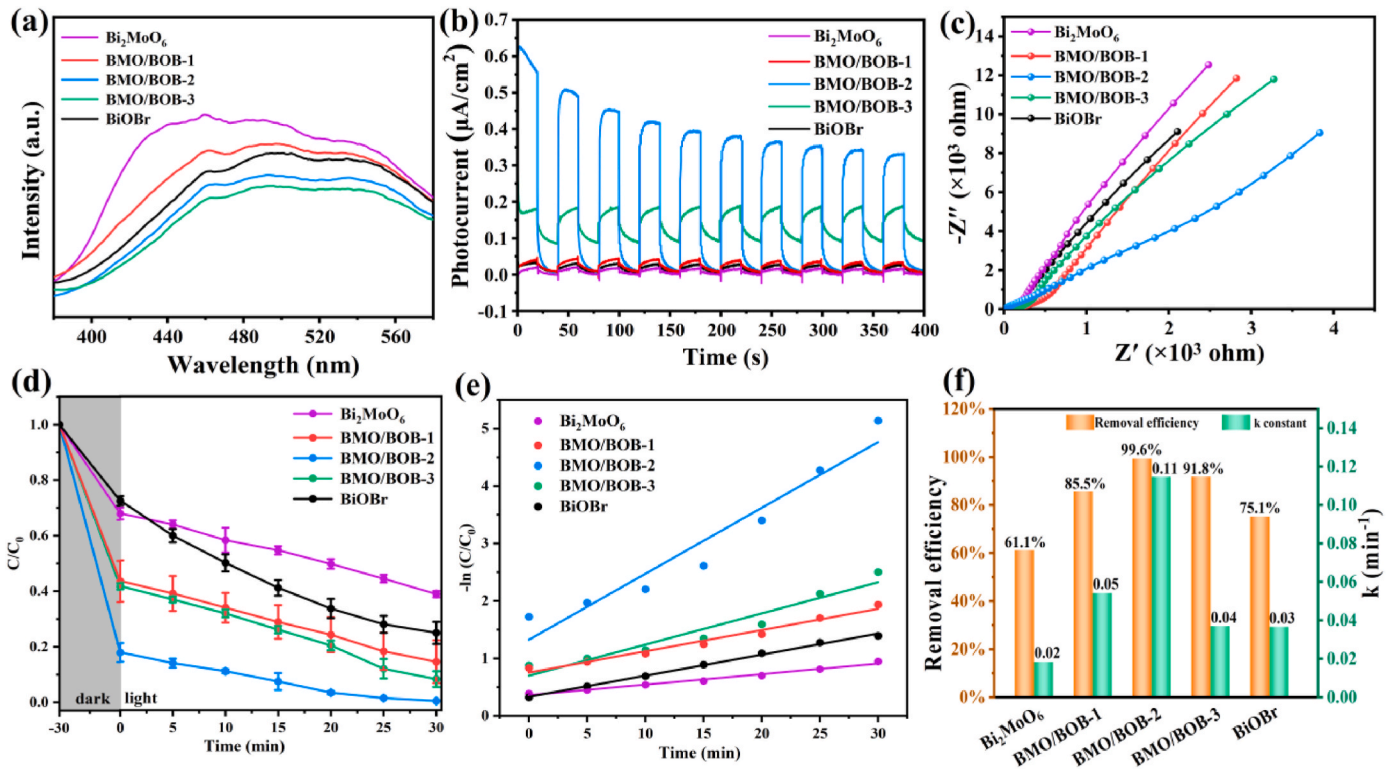

Fig. 4. (a) The steady-state fluorescence spectra (300 nm excitation); (b) Transient photocurrent response curves; (c) Electrochemical impedance curves of samples; (d) The curves of degradation MB under visible light; (e) The corresponding first-order kinetic fitting curves and (f) apparent rate constants.

3.2. Photocatalytic performance evaluation

Taking MB as the research object, the efficiency of the photocatalyst was assessed (Fig. S1). The key factors affecting the photocatalytic performance include the dose of catalyst, the concentration of the solution and the pH value. Figs. S1a–b show the MB removal curves under different catalyst dosage and the corresponding adsorption and photocatalytic removal efficiency. When 5 mg catalyst was added to the reaction system, the adsorption and photocatalytic degradation rate is 63.5% and 16.3%, respectively. When the dosage of BMO/BOB-2 was 10 mg, the adsorption rate reached 86.8%, which indicated that most of the MB was effectively adsorbed on the surface of the catalyst. The photocatalytic degradation rate was 12.8%, which reflected the ability of the catalyst to promote the decomposition of dyes under light irradiation. And the total removal rate is 99.6%. Upon further increase in catalyst dosage to 15 mg and 20 mg, the total removal rate decreased, indicating that the catalyst dosage has a significant effect on the reaction rate. The initial concentration of pollutant solution is investigated in Figs. S1c–d. The result shows the total removal rate of BMO/BOB-2 was the highest among the dye solutions of 10 mg/L. The results show that the removal ability for MB with BMO/BOB-2 attributable to the synergistic interaction between adsorption and photocatalysis.

Meanwhile, the pH value of the liquid is also an essential indicator of the catalytic performance. The initial pH value of the solution was adjusted with 1 mol/L HNO_3 and NaOH solutions. In a certain pH range (pH = 2–10), the degradation performance of BMO/BOB-2 on MB is shown in Fig. S1e. When pH < 5, the degradation efficiency improved as the pH was increased. When pH value is 5, the degradation efficiency reaches 99.6%. When pH > 5, the degradation performance decreased as the pH was increased. There was a significant decrease in degradation efficiency to 68% as the pH was 10. It is demonstrated that the catalyst possesses the optimal photocatalytic performance for pollutant removal under weak acidic conditions. For further studies, the pH of the solution was maintained at 5. Additionally, the degradation ability of 10 mg/L different pollutants with 10 mg catalyst have been studied (Fig. S1f). The degradation performance of BMO/BOB-2 for different pollutants was ranked as MB > TC > RhB > Cr (VI) > MO, within 30 min under visible light.

The synergistic effects of the obtained samples in the adsorption and photocatalytic properties were assessed. Before light irradiation, the suspension containing MB was stirred for 30 min under dark conditions to achieve adsorption-desorption equilibrium. In Fig. 4d, the removal efficiencies of MB by Bi_2MoO_6 and BiOBr were 61.1% and 75.1% after 30 min of illumination, respectively, and all composites showed high activity on MB removal under the same conditions. BMO/BOB-2 exhibited the strongest removal capacity for MB reaching 99.6%. In addition, the adsorption and photocatalytic synergistic removal of MB by BMO/BOB-2 was compared with the catalysts reported in the literature was demonstrated in Table S1. It is observed that the BMO/BOB-2 sample can remove MB in a relatively short time under visible light irradiation, indicating that BMO/BOB-2 could be a promising photocatalyst for MB removal. Fig. 4e shows the first-order kinetic curves corresponding to MB degradation by different catalysts. The MB degradation is guided by a first-order kinetic reaction model. In Fig. 4f, the apparent rate constant K is 11.4×10^{-2} min^{-1} of BMO/BOB-2, which is 6.2 and 3.1 times that of Bi_2MoO_6 and BiOBr, respectively. It can be seen that the formation of Bi_2MoO_6/BiOBr heterostructures can effectively enhance the photocatalytic performance compared to Bi_2MoO_6 and BiOBr.

3.3. Adsorption and photocatalysis synergy

The adsorption process and the adsorption capacity of BMO/BOB-2 for MB before illumination were explored. All samples reached adsorption equilibrium within 30 min, and the adsorption rate of BMO/BOB-2 for MB was 85.9%, significant improvement over Bi_2MoO_6 and BiOBr (Fig. 5a–b). BMO/BOB-2 showed the highest adsorption capacity of 46.8 mg g^{-1} (Fig. 5c), which was 2.75 and 2.87 times of Bi_2MoO_6 and

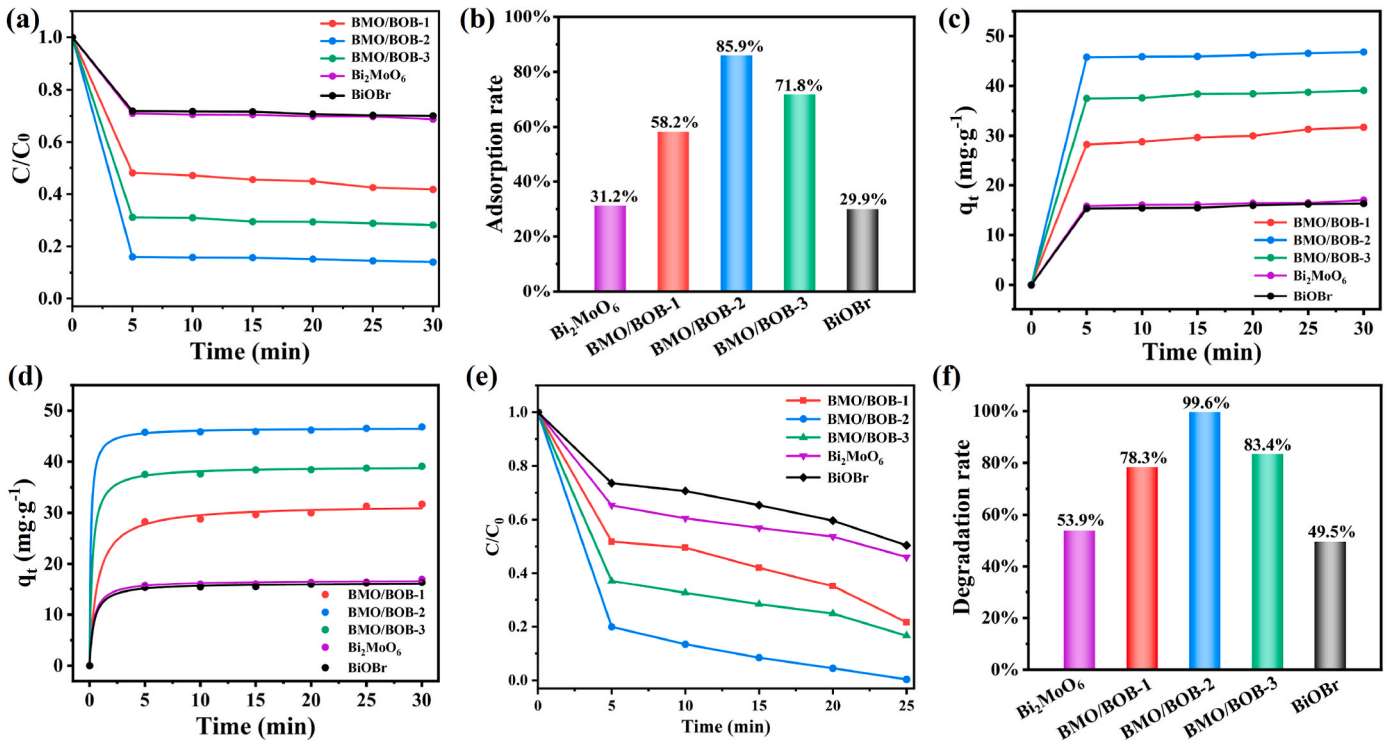

Fig. 5. (a) The adsorption curves, (b) adsorption efficiency, (c) adsorption capacity and (d) the pseudo-second-order kinetic fitting curve of MB on samples; (e) The curves of direct photocatalytic degradation of MB and (f) corresponding degradation efficiencies.

BiOBr, respectively. Adsorption kinetics is one of the methods to describe the adsorption rate and mechanism quantitatively. The adsorption kinetics of MB by the sample was analyzed using a pseudo-second-order kinetic model. As shown in the result, the correlation coefficient of the pseudo-second-order kinetic model (Fig. 5d) was approaching to 1.000, so the adsorption of MB in the BMO/BOB-2 composite was mainly chemisorption, that is, electron transfer may occur between MB molecules and the catalyst. In addition, adsorption equilibrium can also be determined using the Langmuir isotherm model, Freundlich isotherm model and Temkin isotherm model. We can clearly observe the results for c_e/q_e and c_e, ln (q_e) and ln (c_e), as well as q_e and ln (c_e) (Figs. S2a–c). The R^2 value indicates the fitting degree of the adsorption isotherm, and the Langmuir isotherm model shows the highest R^2, indicating that it more accurately describes the experimental data. Therefore, the adsorption process of Bi_2MoO_6/BiOBr composites on MB belongs to the single-layer adsorption on the catalyst surface.

For exploring synergistic effect of adsorption and photocatalysis on MB removal, direct photocatalytic degradation of MB was investigated. In Fig. 5e and f, it can be seen that the degradation rate of MB by BMO/BOB-2 within 25 min is 99.6%, which is close to the removal efficiency of photocatalytic experiment after adsorption equilibrium, but the photocatalytic degradation time is shorter. This may be because the adsorption state of MB on BMO/BOB-2 has not completely saturated, the facilitation effect that exists between MB molecules and photogenerated charges is relatively continuous, thus the efficiency of photocatalytic degradation of pollutants is effectively increased. Therefore, the adsorption equilibrium and photocatalytic experiment show that the removal ability of BMO/BOB-2 composite on MB pollutants is a synergistic effect of adsorption and photocatalysis.

The stability of the catalyst is a major element in the evaluation of photocatalyst. The photocatalytic stability of BMO/BOB-2 composite was evaluated by cycle of the photocatalytic degradation of MB. The degradation efficiency of MB with BMO/BOB-2 remained above 90% after 5 cycles (Fig. S3a), the slightly decrease may be due to the smaller contact area between the photocatalyst and MB molecules caused by adsorption. In order to further demonstrate the micromorphology and structural composition of the sample before and after 5 cycles, SEM and XRD characterization were conducted, as shown in Figs. S3b–c. SEM images showed that the micromorphology of BMO/BOB-2 was still honeycomb remained unchanged before and after 5 cycles. The XRD results show that the position of XRD diffraction peaks before and after the cycle is the same, and there is no deviation. The slight decrease in the intensity of the XRD peaks may be due to a minor decrease in the amount of BMO/BOB-2 sample recovered after 5 cycles. Therefore, the BMO/BOB-2 photocatalyst has good photocatalytic activity and high stability.

3.4. Photodegradation pathway and mechanism analysis of adsorption-photocatalysis

The free radical trapping experiments were performed to determine the active species in the photocatalysis process. The photocatalytic degradation ability decreased when the sacrificial agent was added, and the BQ and EDTA-2Na have the greatest impact. It can be seen that both $\cdot O_2^-$ and h^+ are the main active substances in the reaction (Fig. S3d).

The possible way of removing MB has been further explored by LC-MS (Fig. S4). According to literature reports and test results, there are two possible pathways for MB removal (Du et al., 2022; Krishnan and Shriwastav, 2021; Saha et al., 2018; Wahab et al., 2011; Yang et al., 2023). On the one hand, MB generates an intermediate product m/z = 270 through demethylation, and m/z = 270 is further decomposed into a molecule m/z = 256 with a ternary ring structure. Under visible light irradiation, the intermediate product is further rate-opened and decomposed into m/z = 219, which is further mineralized and decomposed into small molecules. On the other hand, MB is first decomposed into m/z = 274, and then the intermediate products are further ration-opened and decomposed into small molecules, such as m/z = 231, 217, 215, 158, and finally the small molecules are converted into CO_2, H_2O and other inorganic small molecules.

It was investigated the possible attack sites on the MB molecule by DFT calculations. The optimized structure of the MB molecule mainly

consists of benzene ring, 1, 3-cyclohexadiene ring, two dimethylamine groups, N34 and S35 (Fig. 6a). The highest occupied molecular orbital (HOMO) and lowest occupied molecular orbital (LUMO) for MB are shown in Fig. 6b. It is thought that atoms on HOMO are more easily oxidized, while atoms on LUMO are more easily reduced. It can be seen from Fig. 6b that the HOMO orbital of MB is mainly concentrated on the benzene ring, 1, 3-cyclohexadiene ring and N of diamine group, which are the regions where electrons mainly exist. The LUMO orbits are mainly located in the benzene ring, another six-membered ring, N34, S35, N36, and N37, which are concentrated in the positive center (Du et al., 2022). Then, Bi_2MoO_6, BiOBr, Bi_2MoO_6/BiOBr heterojunction and adsorption of MB by heterojunction were calculated (Fig. 6c–f). In Fig. 6c and d Bi_2MoO_6 and BiOBr are both layered structures, consistent with the previous description. The heterojunction formed (Fig. 6e) is favorable for photogenerated carriers migration. The adsorption capacity of MB was significantly enhanced by the formed heterostructures, and the adsorption energy was −3.11 eV, indicating that the adsorption of MB by the prepared Bi_2MoO_6/BiOBr heterojunction sample was spontaneous exothermic (Fig. 6f).

Zeta potential test results of Bi_2MoO_6, BiOBr, and BMO/BOB-2 are shown in Fig. 7a–c. The Zeta potential of BMO/BOB-2 is −4.924 mV, while the Zeta potential of Bi_2MoO_6 is −22.27 mV, indicating that Bi_2MoO_6 is exposed to the interface active site in the composite material, has strong electrostatic adsorption between Bi_2MoO_6 and MB, and has high photocatalytic activity and recycling ability. This is consistent with the DFT calculation results.

The adsorption behavior and mechanism of MB on BMO/BOB-2 were demonstrated by FT-IR spectroscopy. The FT-IR spectra of BMO/BOB-2, BMO/BOB-2 after adsorption and after photocatalysis, as well as MB are shown in Fig. 7d. In the FT-IR spectrum of MB, the characteristic peaks located at 1591 cm^{-1} and 1385 cm^{-1} can be attributed to C=O and C ≡ N, the bands at 1134 cm^{-1} and 1035 cm^{-1} belong to the skeleton vibration of heterocyclic rings in MB (Awais et al., 2022; Chen et al., 2020). The obvious vibration of the Bi-O bond can be observed from the spectrum of BMO/BOB-2. The characteristic peaks of the above two substances appeared in the FT-IR spectra after adsorption and photocatalysis, indicating that MB has strong adsorption on the surface of BMO/BOB-2, during the adsorption-photocatalysis process.

In order to determine the direction of electron transfer in the photocatalysis process, the (010) facet of Bi_2MoO_6 and the (001) facet of BiOBr were selected for work function calculation, as shown in Fig. 7e–f. The work functions of Bi_2MoO_6 and BiOBr are 7.59 eV and 6.97 eV, respectively. Since Bi_2MoO_6 has a lower Fermi level and a larger work function, when Bi_2MoO_6 is in contact with BiOBr, the electrons in BiOBr spontaneously transfer to Bi_2MoO_6 at the interface until the Fermi level reaches equilibrium. Due to the transfer of electrons, the band edges of BiOBr and Bi_2MoO_6 bend upward and downward, respectively. Thus an internal electric field is formed at the interface, and the resulting Bi_2MoO_6/BiOBr composite forms an S-scheme heterostructure.

Based on the above analysis, a collaborative mechanism of adsorption-photocatalysis for S-scheme Bi_2MoO_6/BiOBr heterostructure to removal pollutant was proposed (Fig. 7g). In the initial adsorption process, the electrons and holes on the catalyst surface interact with the MB molecules, showing a high adsorption capacity. The S-scheme heterostructure formed under the action of interfacial electric field after Bi_2MoO_6 contact with BiOBr, which effectively inhibits the photogenerated carrier recombination and enhances the photocatalytic activity. When visible light irradiated, photogenerated e^- and h^+ are produced inside and migrated to the surface of the in the composite, and e^- can reduce the O_2 adsorbed on the surface of the pollutant to $\cdot O_2^-$, the $\cdot O_2^-$ as well as h^+ interact with MB to degrade the pollutant. Eventually, through a synergistic adsorption-photocatalysis, the pollutants are

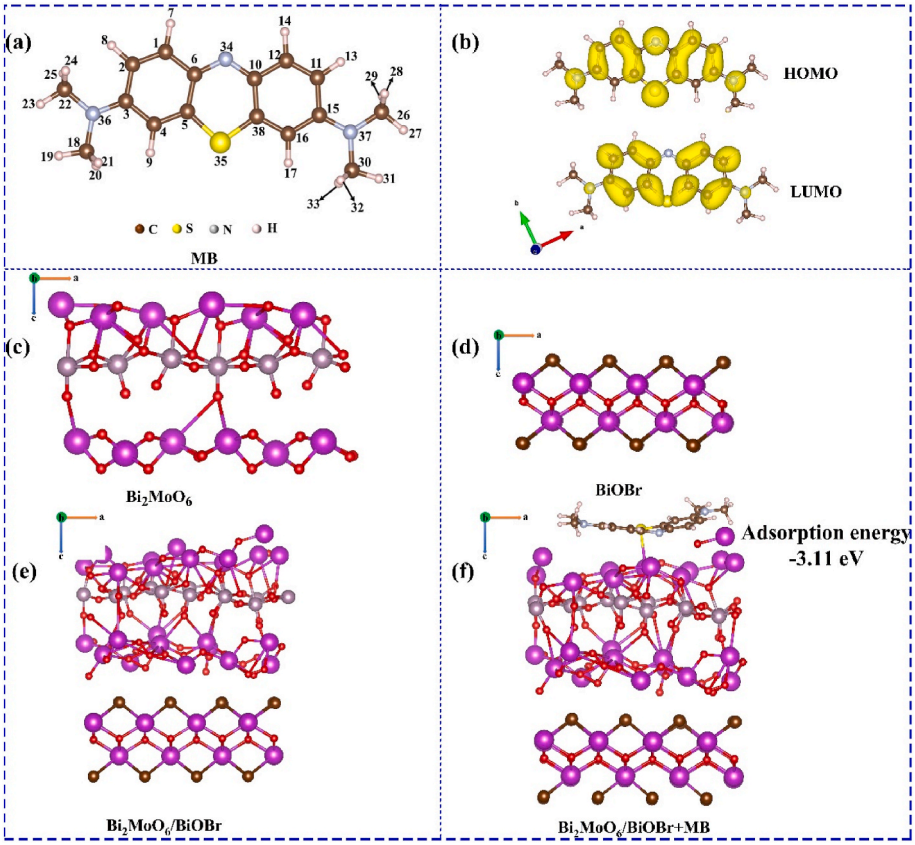

Fig. 6. (a) Optimized molecular structure of MB; (b) HOMO and LUMO of MB; The optimized structure of (c) Bi_2MoO_6, (d) BiOBr, (e) Bi_2MoO_6/BiOBr and (f) Bi_2MoO_6/BiOBr adsorbed MB.

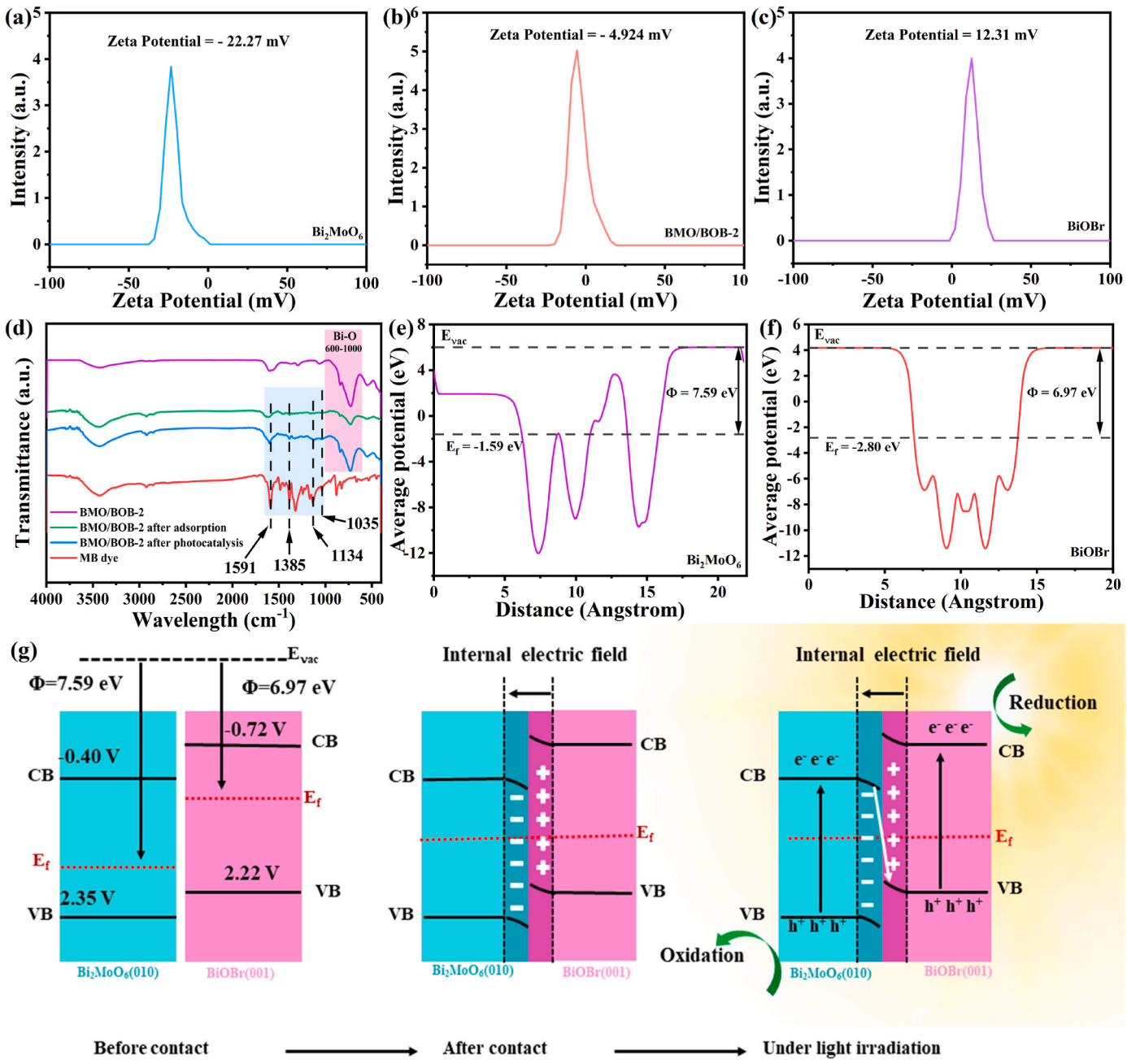

Fig. 7. Zeta potential of (a) Bi_2MoO_6, (b) BMO/BOB-2 and (c) BiOBr; (d) FT-IR spectra of BMO/BOB-2, BMO/BOB-2 after adsorption and photocatalysis, and MB; The work function of (e) Bi_2MoO_6 and (f) BiOBr; (g) Mechanism of adsorption-photocatalytic synergistic pollutant removal by Bi_2MoO_6/BiOBr composites.

reduced to pollution-free small molecules such as CO_2 and H_2O, etc.

4. Conclusion

In summary, the S-scheme Bi_2MoO_6/BiOBr heterostructure were prepared via hydrothermal method by adjusting the amount of $Na_2MoO_4{\cdot}2H_2O$. The prepared BMO/BOB-2 can remove 99.6% of MB, 98.1% of TC, and 86.3% of RhB within 30 min, and the excellent photocatalytic performance attributes to the synergistic effect of adsorption and photocatalysis. The adsorption process of MB on BMO/BOB-2 follows the pseudo-second-order kinetic curve, and the Langmuir isotherm model matches well with the adsorption data. The HOMO and LUMO of MB and the adsorption energy of Bi_2MoO_6/BiOBr composite for MB are demonstrated that the adsorption of MB by Bi_2MoO_6/BiOBr composite is exothermic and spontaneous. The S-scheme interface transfer between Bi_2MoO_6 and BiOBr effectively inhibits the photogenerated carriers recombination and enhances the photocatalytic activity, and the mechanism of adsorption-photocatalysis collaborative removal of pollutants was further proposed. This work is instructive for the synergistic effect of adsorption and photocatalysis of materials to enhance applications in the energy and environmental fields.

CRediT authorship contribution statement

Lili Ai: Writing – review & editing, Methodology, Data curation. **Lijuan Feng:** Writing – original draft, Formal analysis, Conceptualization. **Luxiang Wang:** Writing – review & editing, Supervision, Resources, Project administration. **Yuchun Li:** Methodology. **Chuan Tan:** Investigation. **Manning Zha:** Software. **Dianzeng Jia:** Resources, Project administration. **Nannan Guo:** Methodology.

Declaration of competing interest

The authors declare that they have no known competing financial interests or personal relationships that could have appeared to influence the work reported in this paper.

Acknowledgements

This work was supported by the Natural Science Foundation of Xinjiang Uygur Autonomous Region (2023D01C10), the National Natural Science Foundation of China (22205193 and 52072326), the Central Government Guides Local Scientific and Technological Development Projects of Xinjiang Uygur Autonomous Region (ZZYD2023A06), and the Basic Scientific Research Fund Project for University (XJEDU2022P015).

Appendix A. Supplementary data

Supplementary data to this article can be found online at https://doi.org/10.1016/j.envres.2025.121301.

Data availability

Data will be made available on request.

References

Anwer, A. Mahmood, Lee, J., Kim, K.H., Park, J.W., Yip, A.C.K., 2019. Photocatalysts for degradation of dyes in industrial effluents: opportunities and challenges. Nano Res. 12 (5), 955–972.

Awais, M., Khursheed, S., Tehreem, R., Sirajuddin, Mok, Y.S., Siddiqui, G.U., 2022. pH regulated rapid photocatalytic degradation of methylene blue dye via niobium-nitrogen co-doped titanium dioxide nanostructures under sunlight. Appl. Catal. Gen. 643, 118764.

Bai, X., Wang, Y.J., Li, Y., Wang, X.J., 2019. Adsorption–photocatalytical remediation for series of tetracycline contaminants with BiOCl–CdS composite under simulated sunlight. J. Taiwan Inst. Chem. Eng. 104, 94–105.

Cai, H., Zhang, H., Gao, N., Fang, Y., Xie, X., Fang, Y., Chen, G., 2024. Novel N-ZnO/p-BN adsorption-photocatalytic composites with interfacial bonding for efficient synergistic degradation of pollutants in water. Appl. Surf. Sci. 677, 161060.

Cai, D., Zhang, T., Zhang, F., Luo, X., 2017. Quaternary ammonium β-cyclodextrin-conjugated magnetic nanoparticles as nano-adsorbents for the treatment of dyeing wastewater: synthesis and adsorption studies. J. Environ. Chem. Eng. 5 (3), 2869–2878.

Chen, B., Cao, Y., Zhao, H., Long, F., Feng, X., Li, J., Pan, X., 2020. A novel Fe^{3+}-stabilized magnetic polydopamine composite for enhanced selective adsorption and separation of Methylene blue from complex wastewater. J. Hazard Mater. 392, 122263.

Ding, K., Ai, J., Deng, Q., Huang, B., Zhou, C., Duan, T., Duan, Y., Han, L., Jiang, J., Che, S., 2021. Chiral mesostructured BiOBr films with circularly polarized colour response. Angew. Chem. Int. Ed. 60 (35), 19024–19029.

Dong, G., Han, K., Chen, C., Hu, J., Uvdal, K., 2024. All-organic heterojunctions used for the excellent photocatalytic H_2O_2 synthesis: the key role of bay-position Cl in PDI. Appl. Catal. B Environ. Energy 354, 124144.

Du, Y., Che, H., Wang, P., Chen, J., Ao, Y., 2022. Highly efficient removal of organic contaminant with wide concentration range by a novel self-cleaning hydrogel: mechanism, degradation pathway and DFT calculation. J. Hazard Mater. 440, 129738.

Du, C., He, S., Xing, Y., Zhao, Q., Yu, C., Su, X., Feng, J., Sun, J., Dong, S., 2022. Fabricating S-scheme $BiOBr/Zn_2In_2S_5$ heterojunction for synergistic adsorption-photocatalytic degradation of tetracycline. Mater. Today Phys. 27, 100827.

Han, K., Dong, G., Saeed, I., Dong, T., Xiao, C., 2024. Morphology and photocatalytic tetracycline degradation of g-C_3N_4 optimized by the coal gangue. Chin. J. Struct. Chem. 43 (2), 100208.

Hu, T., Yang, Y., Dai, K., Zhang, J., Liang, C., 2018. A novel Z-scheme Bi_2MoO_6/BiOBr photocatalyst for enhanced photocatalytic activity under visible light irradiation. Appl. Surf. Sci. 456, 473–481.

Jv, A., Wu, L., Lu, J., Feng, B., Che, G., Guan, R., Zhang, Y., Liu, C., Yu, J., Sun, T., 2024. $BiOBr/Bi_2O_2CO_3$ heterojunction photocatalyst for the degradation of tetracycline. ACS Appl. Nano Mater. 7 (11), 12722–12733.

Kang, X., Dong, G., Dong, T., 2023. Oxygen vacancy defect engineering of heterophase junction TiO_2: interfacial/surface oxygen vacancies coadjust the photocatalytic ROS production. ACS Appl. Energy Mater. 6 (2), 1025–1036.

Krishnan, S., Shriwastav, A., 2021. Application of TiO_2 nanoparticles sensitized with natural chlorophyll pigments as catalyst for visible light photocatalytic degradation of methylene blue. J. Environ. Chem. Eng. 9 (1), 104699.

Li, Q., Pan, X., Wang, X., Ma, C., Chen, J., Han, Y., Wang, B., Bo, L., Li, H., Liu, X., Yuan, Y., 2024a. An S-scheme heterojunction BiOBr QDs/$Bi_7O_9I_3$ nanoflowers enabling enhanced photocatalytic oxygen evolution. Catal. Commun. 187, 106843.

Li, L., Zhang, Y., Liu, G., Wei, T., Zhao, J., Wang, B., Ji, M., She, Y., Xia, J., Li, H., 2024b. CoTCPP integrates with BiOBr microspheres for improved solar-driven CO_2 reduction performance. Green Energy Environ. 10 (1), 193–202.

Ling, Y., Zhou, J., Fang, R., Li, Y., Xiao, H., Lei, M., Huang, L., 2024. Fabrication of WO_3 nanorod arrays modified by BiOBr and their enhanced photoelectrocatalytic activity. Sep. Purif. Technol. 337, 126456.

Liu, J., Qin, W., Wang, Y., Xu, Q., Xie, Y., Chen, Y., Dai, Y., Zhang, W., 2024. NH_2-UiO-66 modification BiOBr enhancement photoreduction CO_2 to CO. Sep. Purif. Technol. 344, 127289.

Liu, H., Yu, D., Sun, T., Du, H., Jiang, W., Muhammad, Y., Huang, L., 2019. Fabrication of surface alkalinized g-C_3N_4 and TiO_2 composite for the synergistic adsorption-photocatalytic degradation of methylene blue. Appl. Surf. Sci. 473, 855–863.

Lu, L., Zhang, H., Sun, Z., Wang, J., Wang, H., Xue, J., Shen, Q., Li, Q., 2023. Creation of robust oxygen vacancies in 2D ultrathin BiOBr nanosheets by irradiation through photocatalytic memory effect for enhanced CO_2 reduction. Chem. Eng. J. 477, 146892.

Pang, B., Miao, J., Wang, H., Wu, C., Wu, L., Yuan, G., Wang, X., 2024. Construction of fast charge-transferred 0D/2D $BiOBr/Bi_2WO_6$ S-scheme heterojunction with enhanced photocatalytic performance. Appl. Surf. Sci. 649, 159104.

Qu, Y., Li, X., Zhang, H., Huang, R., Qi, W., Su, R., He, Z., 2022. Controllable synthesis of a sponge-like Z-scheme N,S-CQDs/Bi_2MoO_6@TiO_2 film with enhanced photocatalytic and antimicrobial activity under visible/NIR light irradiation. J. Hazard Mater. 429, 128310.

Saha, D., Desipio, M.M., Hoinkis, T.J., Smeltz, E.J., Thorpe, R., Hensley, D.K., Fischer-Drowos, S.G., Chen, J., 2018. Influence of hydrogen peroxide in enhancing photocatalytic activity of carbon nitride under visible light: an insight into reaction intermediates. J. Environ. Chem. Eng. 6 (4), 4927–4936.

Shen, X., Song, B., Shen, X., Shen, C., Shan, S., Xue, Q., Chen, X., Li, S., 2022. Rationally designed S-scheme heterojunction of C_3N_4/Bi_2MoO_6/carbon fiber cloth as a recyclable, macroscopic and efficient photocatalyst for wastewater treatment. Chem. Eng. J. 445, 136703.

Shen, M., Zhu, X., Lin, L., Li, H., Wang, Y., Liang, Q., Zhou, M., Li, Z., Xu, S., 2025. MOFs-derived S-scheme ZnO/BiOBr heterojunction with rich oxygen vacancy for boosting photocatalytic CO_2 reduction. Sep. Purif. Technol. 353, 128620.

Singh, A., Pal, D.B., Mohammad, A., Alhazmi, A., Haque, S., Yoon, T., Srivastava, N., Gupta, V.K., 2022. Biological remediation technologies for dyes and heavy metals in wastewater treatment: new insight. Bioresour. Technol. 343, 126154.

Sun, Y., Wang, H., Xing, Q., Cui, W., Li, J., Wu, S., Sun, L., 2019. The pivotal effects of oxygen vacancy on Bi_2MoO_6: promoted visible light photocatalytic activity and reaction mechanism. Chin. J. Catal. 40 (5), 647–655.

Wahab, R., Hwang, I.H., Kim, Y.-S., Shin, H.-S., 2011. Photocatalytic activity of zinc oxide micro-flowers synthesized via solution method. Chem. Eng. J. 168 (1), 359–366.

Wang, C., Dang, B., Wang, H., Chen, Y., Yang, Y., Li, Y., Xiong, Y., 2024a. In-plane multiple heterogeneous $Bi_4O_5I_2$/β-Bi_2O_3 nanoflowers with S-type scheme for efficient photocatalytic CO_2 conversion. Chem. Eng. J. 479, 147730.

Wang, H., Yan, C., Xu, M., Li, J., Zhang, Z., Song, X., Liu, X., Huo, P., 2024b. Pd nanoparticle-modified BiOBr/CdS S-scheme photocatalyst for enhanced conversion of CO_2. Inorg. Chem. 63 (37), 17274–17286.

Wu, X., Zhang, F., Niu, L., Liu, J., Li, J., Wang, D., Fan, J., Li, X., Shao, C., Li, X., Liu, Y., 2023. Promoting photocatalytic nitrogen reduction for aqueous nitrogenous fertilizer from organic wastewater over p-BiOBr/n-Bi_2MoO_6 hetero-nanofibers. Chem. Eng. J. 470, 144108.

Xu, X., Meng, L., Dai, Y., Zhang, M., Sun, C., Yang, S., He, H., Wang, S., Li, H., 2020. Bi spheres SPR-coupled Cu_2O/Bi_2MoO_6 with hollow spheres forming Z-scheme Cu_2O/Bi/Bi_2MoO_6 heterostructure for simultaneous photocatalytic decontamination of sulfadiazine and Ni(II). J. Hazard Mater. 381, 120953.

Xu, Y.S., Zhang, Z.J., Zhang, W.-D., 2013. Facile preparation of heterostructured Bi_2O_3/Bi_2MoO_6 hollow microspheres with enhanced visible-light-driven photocatalytic and antimicrobial activity. Mater. Res. Bull. 48 (4), 1420–1427.

Yang, Y., Gu, X., Gong, K., Meng, S., Lei, J., Zheng, X., Feng, Y., Chen, S., 2023. Revealing the charge transfer mechanism and assessing product toxicity in the 2D/1D $Bi_2O_2CO_3$/$Bi_8(CrO_4)O_{11}$ heterostructure system. Environ. Sci. Nano 10 (7), 1867–1882.

Zhao, S.Z., Lu, Y., Lu, R., Hu, Y.-D., Rodriguez, R.D., Chen, J.J., 2023. Constructing $BiOBr/TiO_2$ heterostructure nanotubes for enhanced adsorption/photocatalytic performance. J. Water Process Eng. 54, 103972.

Zhou, L., Xie, M., Su, H., Chen, R., Pang, Y., Lou, H., Yang, D., Qiu, X., 2023. In situ oxidation of ethylene glycol coupled with Bi_2O_3 epitaxial growth to prepare Bi_2O_3/BiOCOOH heterojunctions with oxygen vacancies for efficient photocatalytic lignin degradation. Colloids Surf. A Physicochem. Eng. Aspects. 664, 131134.